

Check for updates

3D Tiled Auxetic Metamaterial: A New Family of Mechanical Metamaterial with High Resilience and Mechanical Hysteresis

Tiantian Li and Yaning Li*

For artificial materials, desired properties often conflict. For example, engineering materials often achieve high energy dissipation by sacrificing resilience and vice versa, or desired auxeticity by losing their isotropy, which limits their performance and applications. To solve these conflicts, a strategy is proposed to create novel mechanical metamaterial via 3D space filling tiles with engaging key-channel pairs, exemplified via auxetic 3D keyedoctahedron-cuboctahedron metamaterials. This metamaterial shows high resilience while achieving large mechanical hysteresis synergistically under large compressive strain. Especially, this metamaterial exhibits ideal isotropy approaching the theoretical limit of isotropic Poisson's ratio, -I, as rarely seen in existing 3D mechanical metamaterials. In addition, the new class of metamaterials provides wide tunability on mechanical properties and behaviors, including an unusual coupled auxeticity and twisting behavior under normal compression. The designing methodology is illustrated by the integral of numerical modeling, theoretical analysis, and experimental characterization. The new mechanical metamaterials have broad applications in actuators and dampers, soft robotics, biomedical materials, and engineering materials/systems for energy dissipation.

I. Introduction

Mechanical metamaterials are engineered materials with artificial structures, targeting specific sets of mechanical properties that cannot be achieved by conventional bulk materials. They have wide applications including structural morphing, [1] energy harvesting, [2] energy absorbing, [3] noise reduction, [4] and shock and impact mitigation. [5] Unusual physical properties emerging from mechanical metamaterials include negative Poisson's ratio, [6] chirality, [7] twisting under compression, [8] negative stiffness, [9] negative coefficient of thermal expansion, [10] and negative refraction; [11] or a combination of them. However, these

T. Li, Y. Li

Department of Mechanical and Industrial Engineering Northeastern University

Boston MA02115, USA E-mail: y.li@northeastern.edu

The ORCID identification number(s) for the author(s) of this article can be found under https://doi.org/10.1002/adma.202309604

DOI: 10.1002/adma.202309604

desired material properties often conflict with each other. For example, strength and toughness,^[12] resilience and hysteresis,^[13] auxeticity and isotropy,^[6a,c] and auxeticity and twisting,^[8] are often mutually exclusive.

Resilience defines the maximum energy absorbed under recoverable deformation, while large energy dissipation occurs mainly through plastic deformation. [14] Thus, engineering materials often possess high resilience but low energy dissipation capability or vice versa. For example, hyperelastic elastomers often have high resilience but with zero mechanical hysteresis. In contrast, ductile metals are able to dissipate large amount of energy through plastic deformation but cannot recover to the original shape beyond very small deformation. Viscoelastic materials can achieve

both as bulk materials but not at the structural level. Therefore, designing a mechanical metamaterial with both high resilience and high energy dissipation capability is challenging. Moreover, prevalent mechanical metamaterials are dominated by cellular/porous designs.^[15] However,

most existing cellular/porous 2D and 3D mechanical metamaterials cannot achieve ideal mechanical isotropy. Very few breaks this trend but only under very small deformation. [16] The bottleneck is that under large deformation, the distortion of ligaments or cell walls will break the initial structural symmetry and therefore the potential mechanical isotropy.

To meet these challenges, we propose and characterize a new family of 3D tiled auxetic metamaterials including isotropic designs, anisotropic designs, and twisting designs. The new metamaterials show remarkable resilience under large deformation together with significant hysteresis under cyclic compressive loading, large tunability, and ideal isotropy in all directions in 3D space and coupled twisting, and auxeticity under uni-axial compression as rarely seen in existing mechanical metamaterials. An integrated experimental, analytical, and numerical approach is applied to quantify the effective mechanical properties of the new designs. Systematic finite element (FE) simulations and analytical analyses are performed. The predictions are verified via mechanical experiments on 3D printed specimens.

www.advmat.de

15214095, 2024,

doi/10.1002/adma.202309604 by Yaning Li

, Wiley Online Library on [30/06/2024]. See

and

on Wiley Online Library for rules of use; OA articles are governed by the applicable Creative

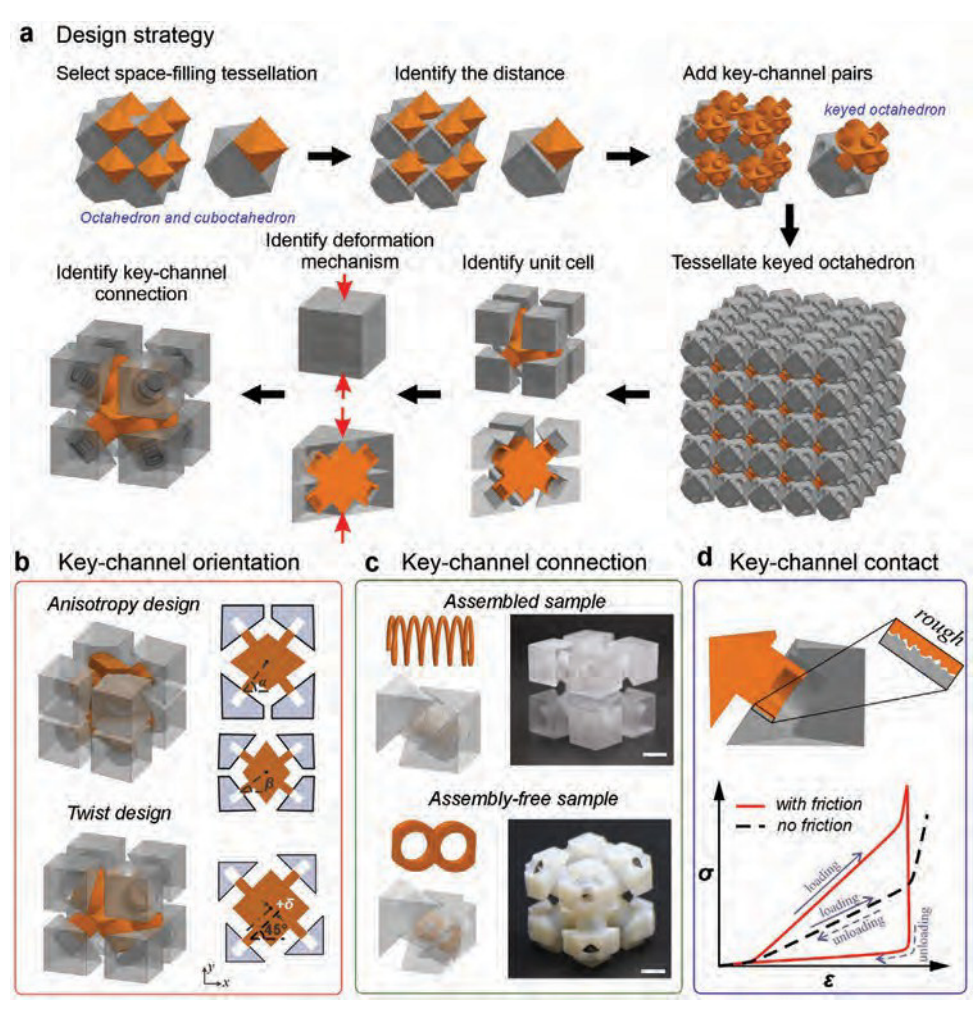


Figure 1. Design strategy and process to construct 3D tiled auxetic mechanical metamaterials. a) The design process, exemplified via keyed tiles of octahedron and cuboctahedron. b) Tune anisotropy and twisting by varying key-channel orientation and location. c) Two types of designs: the assembled sample with spring connection, and the assembly-free sample with double-ring connection. d) Friction induced mechanical hysteresis under cyclic loading.

2. Results and Discussion

2.1. Three-dimensional tiled auxetic metamaterial design

The design process started from selecting a space-filling tessellation template from the family of uniform tiling of Euclidean 3D space. [17] Here, we selected the octahedron and cuboctahedron tessellation as an example to demonstrate the design process. As shown in **Figure 1a**, each cuboctahedron in the tessellation has eight triangular faces and six square faces. Each triangular face of the cuboctahedron is next to one of the triangular faces of a neighboring octahedron. Each square face of the cuboctahedron is next to one of the square face of a neighboring cuboctahedron. After selecting the template, two operations were conducted on the template: 1) neighboring octahedra and cuboctahedra were separated by a certain distance; 2) eight keys were added on each face of octahedra and eight matching channel structures were added on each triangular face of cuboctahedra.

The unit cell or representative volume element (RVE) of the periodic 3D tiled metamaterial is composed of a center keyed octahedron and eight corner pieces, as shown in Figure 1a. Each corner piece is one eighth of a cuboctahedron with a channel structure. To connect the center piece and corner pieces, a connecting architecture will be designed with one end connected to the end of a key on the center piece and the other end connected to the end of a channel on the corner piece. Finally, a 3D keyed-octahedron-cuboctahedron mechanical metamaterial has been designed. Thus, as shown in Figure 1b, the key design factors include the key-channel orientation and location, the key-channel connection type, and the frictional properties of the contact surfaces between the key and channel pairs.

As shown in Figure 1b, by varying the key-channel orientation, mechanical anisotropy can be tuned, and by introducing an offset δ , coupled auxeticity and twisting behavior can be achieved. As shown in Figure 1c, in this investigation, we explored designs with two different types of connection architectures: an

vww.advmat.de

15214095, 2024, 15, Downloaded from https://onlinelibrary.wiley.com/doi/10.1002/adma.202309604 by Yaning Li - Northeastern University , Wiley Online Library on [30062024]. See

the Terms

and Conditions

) on Wiley Online Library for rules of use; OA articles are governed by the applicable Creative Commons

assembled sample with steel springs connecting the keyed tiles and an assembly-free sample with rubbery double-ring connection. The former needs to be assembled manually and the latter can be directly printed via multi-material 3D printing. In addition, as shown in Figure 1d, due to friction between the contact surfaces of keys and channels, the designs are expected to achieve mechanical hysteresis under cyclic loading.

2.2. Deformation mechanism and auxeticity

We started from exploring the representative isotropic design of the assembled sample with springs, as shown in Figure 2a. In the RVE, the key-spring-channels are along 45° with the horizontal direction in all the views of x-y, y-z, and x-z planes. The diameter and length of the spring are d_0 = 5.5 mm, l_0 = 9.4 mm, respectively. As shown in Figure 2b, the RVE of the assembled design includes three parts (Section S1, Supporting Information): the first part is the rigid center octahedron (orange) with eight cylindrical key-channel attached to each of its eight faces; the second part includes the eight rigid corner pieces (grey) with cylindrical engraved caps; the third part includes eight metal springs. The two rigid parts form eight channels perpendicular to each face of the center octahedron. The three parts are assembled by installing each spring in each channel to connect the two rigid parts. The diameter of the key is d_1 = 6.5 mm, the diameter of the channel is D_1 = 9 mm, and the length of the channel is L_1 = 7 mm. Thus, the 3D mechanical metamaterial with body-centered cubic (BCC) symmetry is created. The rigid parts are fabricated via a 3D printer (Stratasys, Connex3) by using the VeroClear material (transparent, polymethyl methacrylate) in the printer. The specimen of the RVE is generated by assembling the 3D printed rigid parts and eight springs (steel, McMaster, 94125K422), as shown in Figure 1b. The initial length of the spring is 9.4 mm, and the spring stiffness $k = 1.16 \text{ N mm}^{-1}$. The overall dimension of the 3D printed specimen is 30 mm × 30 mm × 30 mm.

For the assembly-free design, the steel springs in the assembled design are replaced with rubbery double-ring structures, as shown in Figure 2c. The diameter of the channel D_2 = 10 mm, the length of the key is L_2 = 7 mm. The specimen of assembly-free design is fabricated via the same 3D printer with multimaterial printing by using the VeroWhite material (white, polymethyl methacrylate) for the rigid parts and TangoBlack material (black, rubbery) for the soft double-rings. To facilitate the removing of the supporting materials inside the samples after printing, three cylindrical holes with radius r = 4 mm are added on each corner piece.

Both specimens are compressed uniaxially on an Instron (Model 9400) material testing machine with a 500 N load cell. To reduce friction, lubrication oil is applied on the bottom and top surfaces of the specimen and the compression plates. For the assembled sample, the effective engineering stress–strain curves and the curves of the effective Poisson's ratio from the experiment (Video S1, Supporting Information), FE simulation, and an analytical model (Section S2, Supporting Information) are compared in Figure 2d. It can be seen that the experimental, numerical, and analytical results match very well. During the overall compressive deformation, contact between parts occurs twice (C1 and C2): the first contact C1 occurs at $\approx 3\%$ overall compressive

strain, when the keys are in contact with the channel walls, as shown in Figure 2e; and the second contact C2 occurs at \approx 21% overall compressive strain, when the keys are in contact with the end of the channel, as shown in Figure 2e.

For the assembled sample, the two contact events separate the deformation into three stages (Stages I, II, and III shown in Figure 2d): Stage I, before the first contact C1, the stress-strain curves show a very low slope and the effective Poisson's ratio is positive, ≈0.2; Stage II, after the first contact C1 and before the second contact C2, the stress-strain curves show an increased constant slope and the effective Poisson's ratio dramatically drops to -1 and is kept unchanged during this stage; Stage III, after the second contact C2, the stress-strain curves show a large increase in slope and the effective Poisson's ratio also increases to \approx 0.33. The experimental snapshots i. ii. and iii representing the deformed configuration in each stage are shown in Figure 2e. Evidently, the specimen shows large auxeticity in Stage II. The auxetic behavior in Stage II is because of that the deformation of the spring is kinematically constrained by the key-channel of the rigid components, and there is relative sliding between the keys and the channels. This mechanism is similar to the keyed-brick mechanism explained by Evans and Alderson.[9a,18] Through the sliding and the spring deformation, the eight rigid corner pieces are brought in together toward the center octahedron, showing an overall negative Poisson's ratio.

For the assembly-free sample, similar mechanical behaviors were observed. The effective engineering stress-strain curves and the curves of the effective Poisson's ratio from the experiment (Video S3, Supporting Information), FE simulation, are compared in Figure 2f. Again, the curves show three stages including stage I and II as the same deformation mechanism with that of assembled sample. While at stage III, the assembly-free sample shows a decreased stress due to the damage in one of the soft rubber rings. Stress/strain contours of the hard pieces/the rings are shown in Figure 2g. Moreover, the Poisson's ratio gradually decreases to -1 which is different with the assembled sample. This is because in the assembled sample, the deformation of steel spring is uni-directional while in the assemblyfree sample, the deformation of rubbery rings has both inplane and small out-of-plane components which induce slight key rotation.

2.3. Resilience and hysteresis

The resilience and the energy dissipation capability of 3D keyed-octahedron–cuboctahedron metamaterial are characterized via cyclic loading–unloading uni-axial compression experiments. The assembled sample is cyclically loaded to strains of 0.075, 0.125, 0.175, and 0.21 sequentially and unloaded after through total four cycles (Video S2, Supporting Information). Thus, the cyclical loading covers Stages I and Stage II. The overall engineering stress–strain curves from experiments, FE simulations, and the analytical model match well, as shown in **Figure 3**a.

Interestingly, Figure 3a shows that after each loading cycle, the deformation is not only fully recovered to its original configuration but also with very high hysteresis in Stage II, indicating both high resilience and high energy dissipation capability, which are two desired mechanical properties often conflicting to each

15214095, 2024, 15, Downloaded from https://onlinelibrary.wiley.com/doi/10.1002/adma.202309604 by Yaning Li - North

stern University, Wiley Online Library on [30/06/2024]. See the Terms

and Condit

nditions) on Wiley Online Library for rules of use; OA articles are governed by the applicable Creative

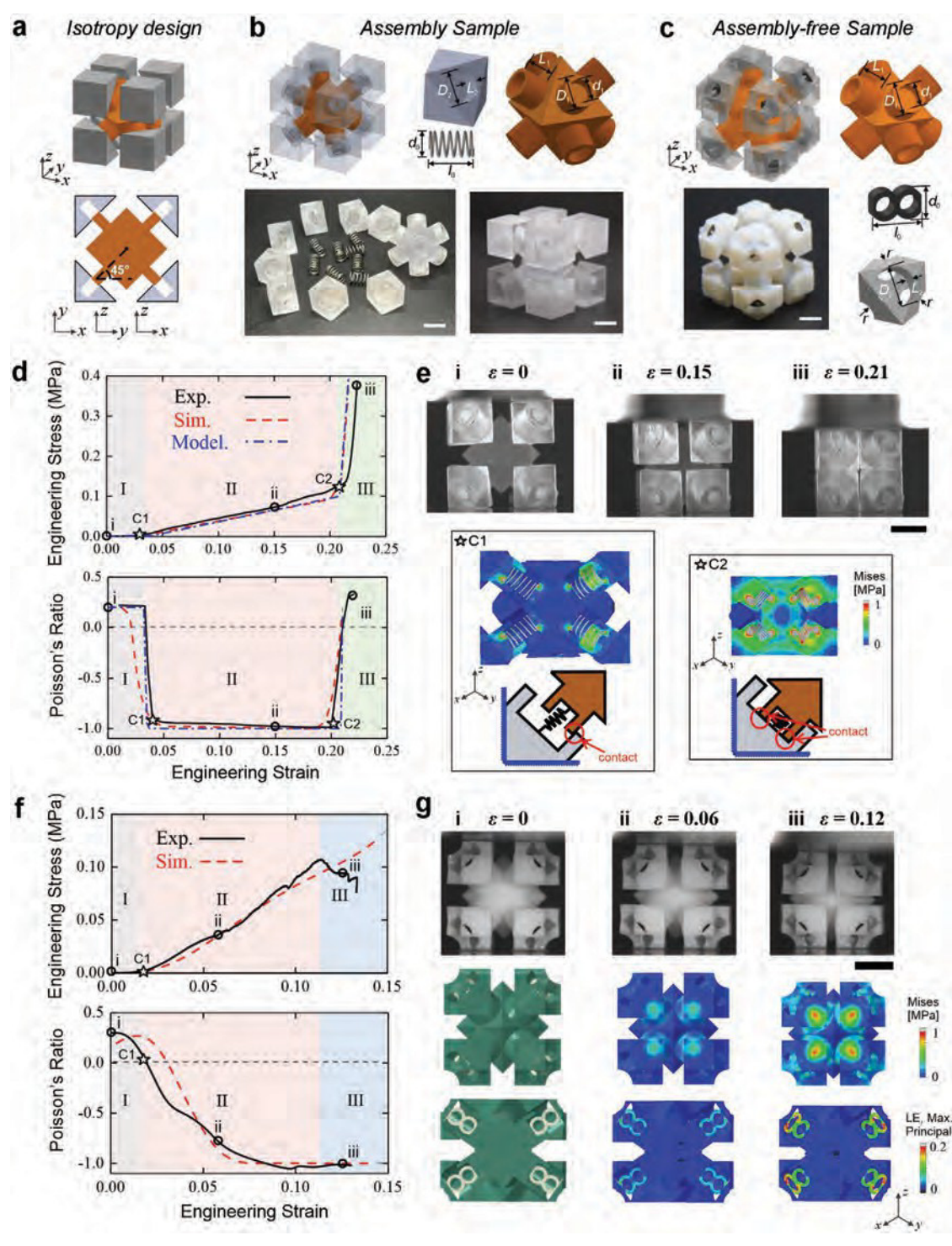


Figure 2. The representative isotropic design of 3D keyed-octahedron—cuboctahedron metamaterial shows an effective Poisson's ratio of –1 under uniaxial compression. a) The periodic 3D isotropic design and the RVE with BCC symmetry, in all the views of *x*–*y*, *y*–*z*, and *x*–*z* planes, the key-spring—channel is 45° along the horizontal directions. b) The geometry and the specimen of the assembled design with springs. c) The geometry and the specimen of the assembly-free design. d,f) Experimental, numerical, and analytical engineering stress—strain curves, and the curves of the effective Poisson's ratio versus engineering strain for the assembled sample and the assembly-free sample, respectively. e,g) Experimental snapshots of the specimen at different overall engineering strains in uni-axial compression experiment (Scale bar, 10 mm) and FE von-Mises stress contours of the specimen with deformed configuration during FE simulations for the assembled design and assembly-free design, respectively. and the corresponding schematics at the two contact points, C1 and C2 shown in (d).

www.advmat.de

15214095, 2024, 15, Downloaded from https://onlinelib

doi/10.1002/adma.202309604 by Yaning Li - Nort

tern University, Wiley Online Library on [30/06/2024]. See the Term

on Wiley Online Library for rules of use; OA articles are governed by the applicable

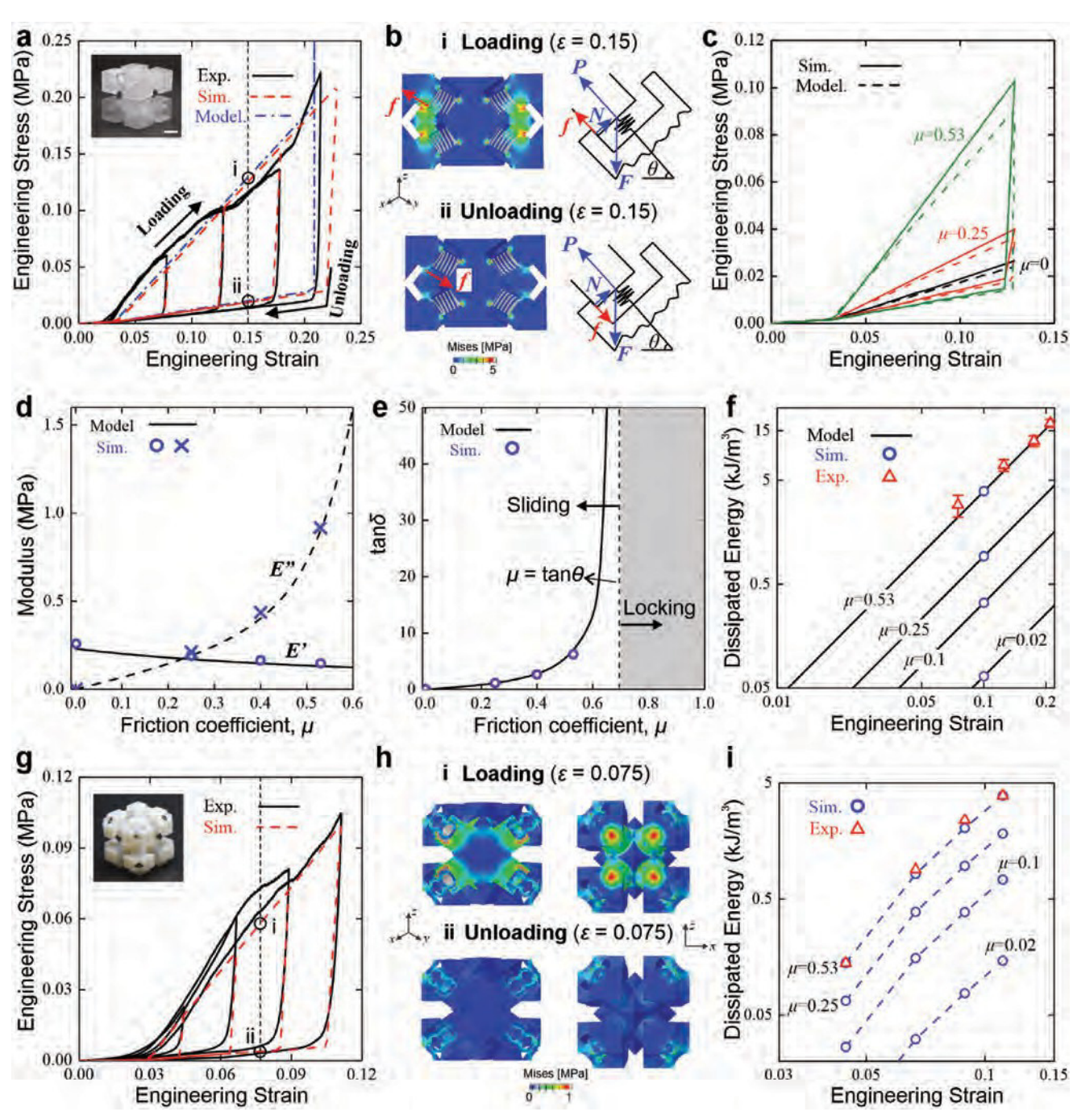


Figure 3. The representative isotropic design of 3D keyed-octahedron—cuboctahedron metamaterial shows high resilience and large hysteresis under cyclic loading—unloading. For assembled samples, a) engineering stress—strain curves from experiments, FE simulations, and the analytical model. b) FE von-Mises stress contours and free body diagrams for loading stage and unloading stage at the same 15% overall compressive strain (the friction force changes direction from loading to unloading). c) FE and analytical stress—strain curves for models with different friction coefficients of 0, 0.25, and 0.53. d) Storage modulus E' and loss modulus E' as functions of friction coefficient. e) The evolution of damping ratio $\tan \delta$ with friction coefficient μ and the critical μ^* for transition between sliding and locking behaviors. f) The evolution of energy dissipation as a function of engineering strain for different friction coefficients μ = 0.02, 0.1, 0.25, and 0.53. For assembly-free samples, g) engineering stress—strain curves from experiments and FE simulations. h) FE von-Mises stress contours for loading stage and unloading stage at the same 15% overall compressive strain. i) The evolution of energy dissipation as a function of engineering strain for different friction coefficients μ = 0.02, 0.1, 0.25, and 0.53.

15214095, 2024, 15, Downloaded from https://onlinelibrary.wiley.com/doi/10.1002/adma.202309604 by Yaning Li - Northeastern University . Wiley Online Library on [30.062024]. See the Terms and Conditions (https://onlinelibrary.wiley.com/term/

-and-conditions) on Wiley Online Library for rules of use; OA articles are governed by the applicable Creative Commons

other. To explore the influences of friction coefficients between the parts, FE predictions of the engineering stress-strain curves for models with various friction coefficients $\mu = 0$, 0.25, and 0.53 are compared in Figure 3c. It can be seen that when $\mu = 0$, the effective stiffness in loading and unloading process is the same. indicating zero hysteresis. When μ increases, the effective stiffness in Stage II in the loading process increases, while it dramatically decreases in the unloading process. Thus, the hysteresis is due to friction, and it increases with friction coefficient.

The difference in the effective stiffness in loading and unloading process is because of the change in direction of the friction forces, as schematically shown in Figure 3b. FE simulations further proved that when unloading starts, the friction force immediately changes to the opposite direction, making the overall compressive force suddenly drops to a low level and then linearly decreases until all energy stored in the springs is released. The effective stiffness of the design in the loading and unloading stages is derived from the analytical model (Section S2, Supporting Information) as

$$E(\text{loading}) = \frac{2k}{a \sin \theta (\sin \theta - u \cos \theta)} \tag{1}$$

$$E(\text{loading}) = \frac{2k}{a \sin \theta (\sin \theta - \mu \cos \theta)}$$

$$E(\text{unloading}) = \frac{2k}{a \sin \theta (\sin \theta + \mu \cos \theta)}$$
(2)

where k is the spring constant, a is the edge length of the RVE, and slant angle θ shown in Figure 3b is the angle between the key-channel and the horizontal direction measured in the diagonal cross section. For the representative isotropic design with

cubic symmetry, the angle $\theta = \arcsin(1-3)$. Equation (1) shows that when the friction coefficient $\mu \ge \tan \theta$, the effective stiffness in the loading process will go to negative, indicating a locking behavior. Thus, $\mu^* = \tan \theta$ is the upper limit of the friction coefficient to ensure the sliding between the key and channel and therefore the deformation of the springs inside.

The hysteresis in Stage II produces damping. Thus, to quantify damping, the storage modulus E' is defined as the modulus in the unloading process, that is, E' = E(unloading), and the loss modulus E'' is defined as the difference of the modulus in loading and unloading process, that is,E'' = E(loading) - E(unloading). According to Equations (1) and (2), when the friction coefficient increases, the storage modulus dramatically increases while the loss modulus slightly decreases. This is proved via both FE and analytical modeling, as shown in Figure 3d. The damping ratio $tan\delta$ is defined as the ratio of the area between the loadingunloading curves to that under the loading curve. According to Equations (1) and (2), the damping ratio ($\tan \delta$) in Stage II is de-

$$\tan \delta = \frac{E''}{E'} = \frac{2\mu \cos \theta}{\sin \theta - \mu \cos \theta}$$
(3)

Equation (3) is plotted in Figure 3e and verified by the FE simulations. It shows that the damping ratio increases from 0 to infinity when the friction coefficient increases from 0 to $\tan \theta$. When $\mu \le$ $\tan \theta$, due to the keyed-brick mechanism, the key-channel pairs will have relative sliding and the springs will be compressed. However, when $\mu \ge \tan \theta$, key-channel pair is locked and the springs inside cannot be deformed, indicating a rigid mode for the design. In one loading cycle, the hysteresis area between the loading-unloading curves represents the energy dissipation U_{i} which can be derived as a function of the applied overall strain ϵ

$$U(hysteresis) = \frac{2k\mu \cot \theta}{a(\sin^2 \theta - \mu \cos^2 \theta)} (\varepsilon - \varepsilon)^2$$
(4)

where ϵ_{c1} is the overall strain at the first contact C1. Equation (4) is plotted as a logarithm graph in Figure 3f and verified via both FE simulations and experiments. The energy dissipation capability increases with the friction coefficient.

The assembly-free sample is cyclically loaded to strains of 0.044, 0.066, 0.088, and 0.11 sequentially and unloaded after through total four cycles (Video S4, Supporting Information). Figure 3g shows that after each loading cycle, the deformation is not only fully recovered to its original configuration but also with very high mechanical hysteresis, indicating both high resilience and high energy dissipation capability. Similarly, FE simulations (Figure 3h) further proved that when unloading starts, the friction force immediately changes to the opposite direction, making the overall stress drops to a low level and then decreases until all energy stored in the rubber circles is released. Again, Figure 3i shows that the energy dissipation capability increases with the friction coefficient.

2.4. Ideal isotropy

The assembled design with springs is expected to show ideal isotropy. To verify this hypothesis, FE simulations are performed to determine three independent elastic constants^[16c] of the assembled design (details in Section S3, Supporting Information). The arbitrary loading direction is defined as a vector [hkl] in the global cartesian coordinate system x-y-z, as shown in **Figure 4**a. From three FE simulations under uniaxial compression, pureshear, and hydrostatic compression, the three components of the compliance matrix, S_{11} , S_{12} , and S_{44} are obtained as S_{11} = 2.04 $(MPa)^{-1}$, $S_{12} = 1.98$ $(MPa)^{-1}$, and $S_{44} = 0.13$ $(MPa)^{-1}$. Due to the cubic symmetry of the design, the effective stiffness and the effective Poisson's ratio in an arbitrary loading direction can be calculated.[19] Details of the calculation method can be found in the Section \$4 (Supporting Information). The results are shown in Figure 4. While for the assembly-free design with double-ring structures, since the double-ring structure has a 2D geometry, we do not expect it to be ideally isotropic, although it could potentially be ideally isotropic as well, if a 3D symmetric design is employed.

As shown in Figure 4a, the effective Poisson's ratio v_{ii} of the design in an arbitrary loading direction [hkl] can be measured in a local coordinate system x'-y'-z'. The subscript i represents the loading direction, which is along z' direction represented as vector [hkl] in x-y-z global coordinate system, and the second subscript *j* represents the direction of the lateral strain measured. Angle φ defines the direction j, as an angle in the x'-y' plane. The effective Poisson's ratio v_{ii} are plotted as a function of φ in a polar graph for selected loading direction [hkl], as shown in Figure 4b,c. In the three most important loading directions, uniaxial direction [001], plane diagonal direction [011], and body diagonal direction [111], the effective Poisson's ratios are between

15214095, 2024, 15, Downloaded from https://onlinelibrary.wiley

om/doi/10.1002/adma.202309604 by Yaning Li

, Wiley Online Library on [30/06/2024]. See

the Terms

and Conc

on Wiley Online Library for rules of use; OA articles are governed by the applicable

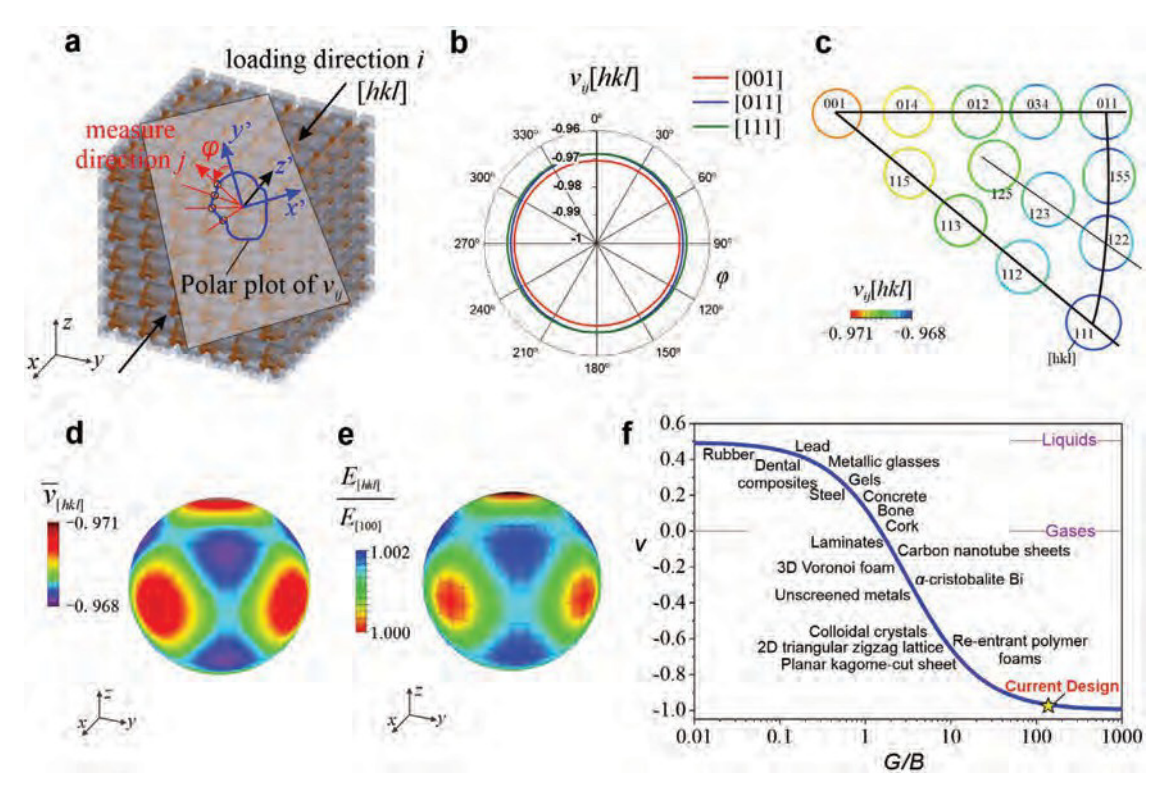


Figure 4. The representative isotropic design of 3D keyed-octahedron—cuboctahedron metamaterial achieves ideal mechanical isotropy. a) Schematics illustrating the effective Poisson's ratio v_{ij} of the design measured under loading in an arbitrary loading direction i, defined by [hkl] in the global coordinate system x-y-z, and along direction j defined as angle φ in the plane perpendicular to the loading direction. b) FE results of the effective Poisson's ratios in a polar plot measured under three orthogonal loading directions of [001], [011], and [111], respectively. c) FE polar plots for the effective Poisson's ratios in 14 different loading directions. d,e) The average effective Poisson's ratio (d) and the normalized effective moduli (e) in all different loading directions in a 3D space. f) The curve of the Poisson's ratio versus the ratio G/B of the shear modulus to the bulk modulus for ideal isotropic continuums, and the data for existing materials, $^{[6a,16a,20]}$ and the data for the current design.

-0.96 to -0.97, as shown in Figure 4b. Figure 4c shows the effective Poisson's ratios are superimposed on the standard triangle of the stereographic projection and in all 14 arbitrarily selected loading directions, indicating high isotropy with values between -0.968 to -0.971. The average effective Poisson's ratio under loading direction i can then be calculated via averaging the measured results in the corresponding polar plots. Figure 4d,e shows the FE results of the average effective Poisson's ratio and the normalized modulus in all different directions. The spherical profile of the plots in Figure 4d,e clearly illustrates that both the effective Poisson's ratio and the effective stiffness of the design are ideally isotropic, that is, having the same values in any direction.

Based on the classic continuum mechanics, for ideal isotropic continuum, the ratio of the shear modulus to bulk modulus is related to the Poisson's ratio as $G = 3(1 - 2\nu)(1 + \nu)$. Thus, for ideal isotropic material, when the Poisson's ratio reaches -1, the G/B ratio will go to infinity. However, for existing isotropic materials, G/B ratio can only reach to less than 19.5, when the Poisson's ratio of them[6a,16a,20] reaches larger than -0.8. For the current design, from FE simulations, the effective shear modulus G = 7.69 MPa, the bulk modulus B = 0.056 MPa, and the ratio G/B = 138, which is about one order of magnitude higher than that of existing ones. Thus, in this sense, the current design is pushing toward the theoretical limit.

For isotropic material, the shear stiffness, G = E/2(1 + v), where E is Young's modulus. The indentation stiffness is proportional to $E/(1 - v^2)$. The mode I (opening) fracture stress of a structure from a pre-existing flaw is proportional to

 $^{\nu}$ $_{\nu}$ $_{\nu}$ $_{\nu}$ $_{\nu}$ $_{\nu}$ $_{\nu}$ $_{\nu}$ $_{\nu}$ is the fracture surface energy, and a is the critical flaw size. [6a] Even if the material is compliant, provided the Poisson's ratio ν is closed to the thermodynamic limit of –1, it is still hard to be sheared, indented or fractured. Our designed metamaterial can reach the theoretical limit of isotropic negative Poisson's ratio, –1. Therefore, the new auxetic tiled designs are excellent candidates for applications targeting enhanced shear resistance, indent resistance, or fracture toughness.

2.5. Tunable anisotropy

By taking the assembled design as an example, based on the isotropic design, anisotropic designs with tuned mechanical anisotropy can be created by varying the two projection angles α and β (shown in **Figure 5a**) of the key-channel on the x-y plane and x-z plane, respectively. For the previous representative isotropic design, $\alpha = \beta = 45^\circ$. By choosing $\alpha = 27^\circ$, $\beta = 14^\circ$, an anisotropic design is generated and fabricated via the 3D printer (Connex 3) with the same springs installed inside as shown in Figure 5a. Three uniaxial compression tests on three orthotropic

www.advmat.de

15214095, 2024, 15, Downloaded from https://onlinelibrary.wiley

doi/10.1002/adma.202309604 by Yaning Li

stern University, Wiley Online Library on [30/06/2024]. See

and

on Wiley Online Library for rules of use; OA articles are governed by the applicable Creative

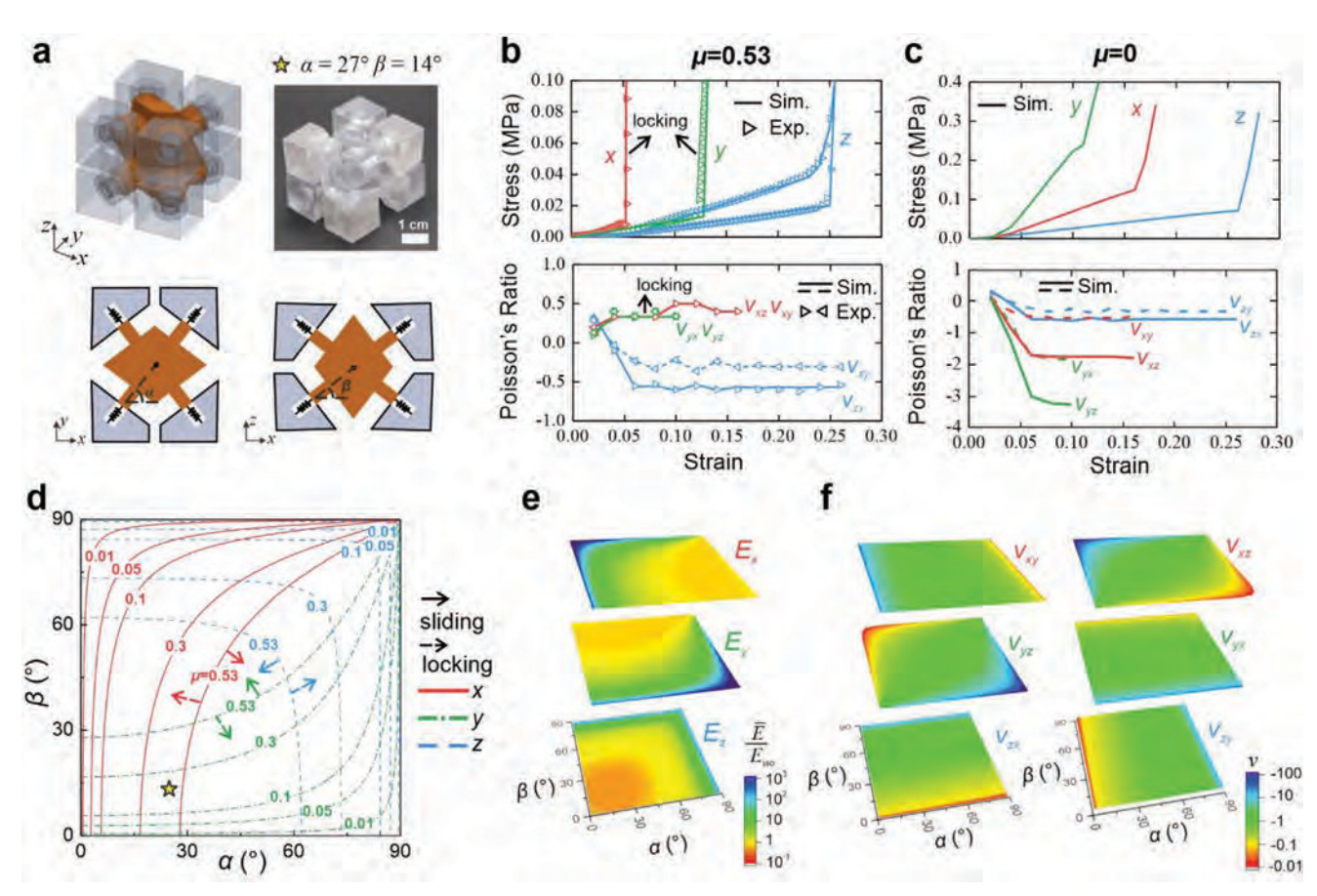


Figure 5. Anisotropic designs of 3D keyed-octahedron–cuboctahedron metamaterial with widely tuned mechanical anisotropy. a) Schematics illustrating the two projection angles α and β of the key-channel on the x-y plane and x-z plane, respectively, and the assembled specimen. b) The experimental and FE engineering stress–strain curves and the measured effective Poisson's ratios in three loading directions x, y, and z, respectively, for friction coefficient of 0.53, and c) for comparison, the same set of FE curves for the case with friction coefficient of 0. d) A map shows the design spaces for sliding or locking behaviors with different parameter (α, β, μ) . e) FE prediction of the effective stiffness and f) the effective Poisson's ratios in three orthogonal directions.

directions (x, y, and z) are performed on the specimen. Results from the experiments and corresponding simulations agree well, which are shown in Figure 5b.

As shown in Figure 5b, in both experiments and FE simula-

tions, the specimen shows locking behavior when compressed along x and y directions, respectively, and shows sliding behavior when compressed along direction z. When compressed in x and y direction, right after Stage I, the stress dramatically increases after the first contact, indicating the locking between keys and channels. The effective Poisson's ratios measured are around 0.33 which is similar to that of the 3D printed material. While when compressed in direction z, due to the sliding behavior, the hysteresis effects are observed in stage II. The measured Poisson's ratios are v_{zx} = -0.57 and v_{zy} = -0.33. Moreover, for comparison, FE simulations on the same design with $\mu = 0$ are also performed and the results are shown in Figure 5c. It can be seen that the design shows sliding behaviors and therefore negative Poisson's ratio when compressed in all three directions. The Poisson's ratios when loaded in x, y, and z directions are $v_{xy} = -0.51$, $v_{xz} = -1.76$, $v_{yx} = -1.83$, $v_{yz} = -3.23$, $v_{zx} = -0.33$, and $v_{zy} = -0.57$, respectively. The stress–strain curves show the three stages and zero hysteresis.

For the anisotropic designs, the critical friction coefficients for the locking behavior vary in x, y, and z directions and can be calculated analytically as $\mu^* = \tan \theta_x = \sqrt{\frac{z}{\tan^2 \theta_x \tan \theta_y}}$, $\mu^* = \tan \theta_y = \sqrt{\frac{z}{\tan^2 \theta_y \tan \theta_y}}$

 $\sqrt{\tan \alpha}$ and $\mu_z^* = \tan \theta_z = \tan \beta \cos \alpha$, respectively. Thus, a map of the design space for locking or sliding behaviors in all three directions can be plotted in Figure 5d. It shows that when $\mu=0$, there is no locking zone, the design can slide when compressed in all three directions. As shown in Figure 5d, for a certain non-zero friction coefficient, the area between the three colored lines indicates the design space for sliding in all three directions. Outside this area, the design will lock either in x and/or y and/or z directions. It can be seen that when the friction coefficient increases, the design space for sliding shrinks, and the design space for locking increases.

The effective modulus and the effective Poisson's ratio for the anisotropic design can be derived analytically as well (details in Section S5, Supporting Information). At μ = 0, the FE predicted effective moduli and the effective Poisson's ratios in three orthotropic directions for various geometry parameters (α , β) are shown in Figure 5e,f, respectively. It can be seen that by changing α , β between 0° and 90°, the effective moduli and the effective

15214095, 2024, 15, Downloaded from https://onlinelibrary.wiley.com/doi/10.1002/adma.202309604 by Yaning Li - Norther

astern University, Wiley Online Library on [30/06/2024]. See

the Terms

and Condit

on Wiley Online Library for rules of use; OA articles are governed by the applicable Creative

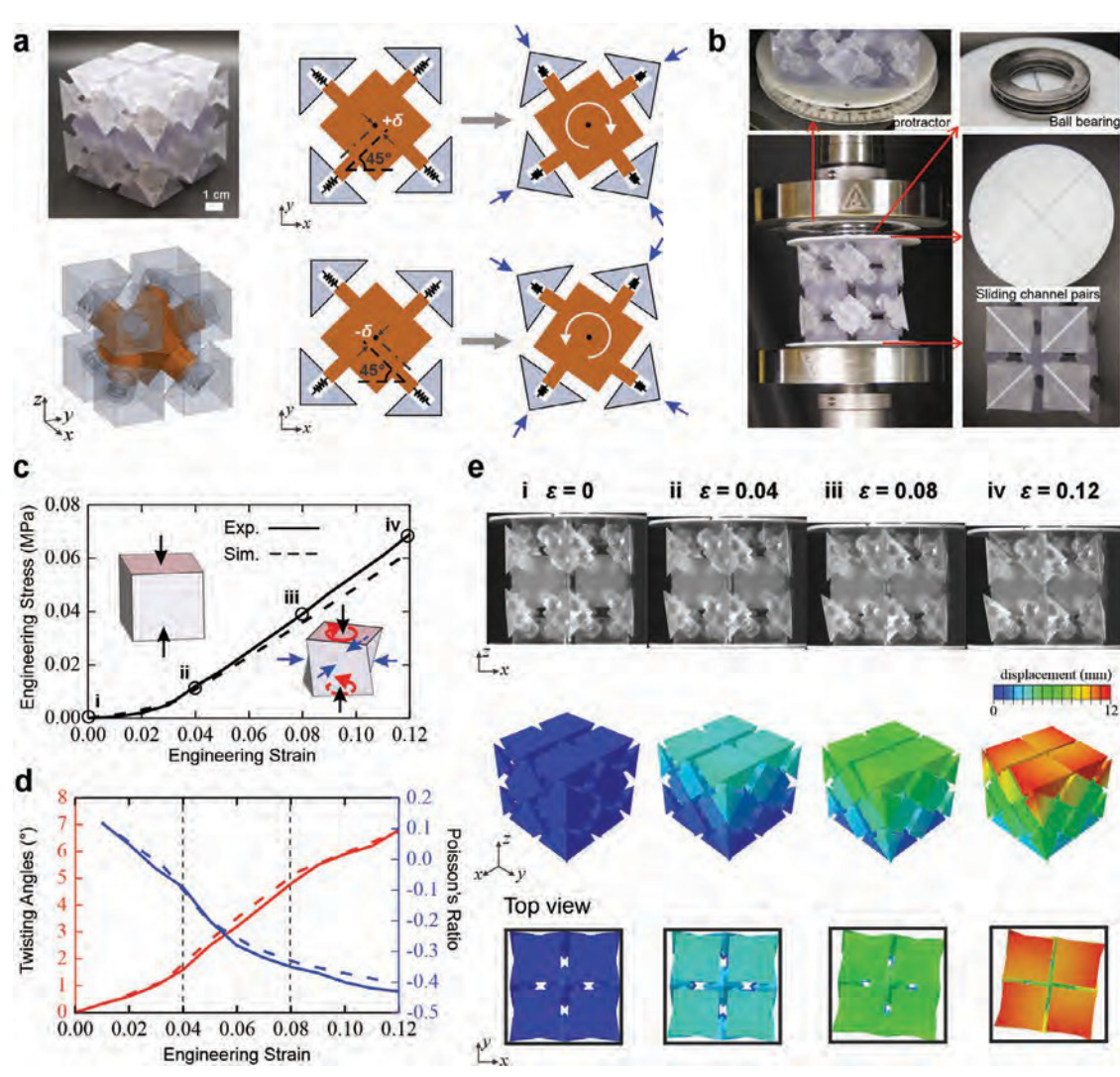


Figure 6. The rotationally symmetric design of 3D keyed-octahedron—cuboctahedron metamaterial with simultaneous twisting and auxeticity. a) The specimen and schematics illustrating the design strategy, offset δ, and the torque. b) Experimental set-ups to measure the twisting and shrinkage, including a ball bearing for free z-rotation on the top surface, and a protractor to measure the twist angle, and the 3D printed sliding channels to constrain z-rotation while allow in-plane shrinkage on both top and bottom surfaces. c) Experimental and FE engineering stress—strain curves, and d) the curves of the twisting angle, and the effective Poisson's ratio as a function of the engineering strain. e) Snapshots from the experiments and FE simulations at the overall compressive strains of 0, 0.04, 0.08, and 0.12, from i–iv, respectively (the square frames on the bottom row represents the profile of the undeformed configuration).

Poisson's ratios can be tuned by orders of magnitude in all three directions.

2.6. Simultaneous twisting and auxeticity

The isotropic and anisotropy designs are symmetric about the x–z, and y–z planes. If the symmetry is changed, interesting new properties can be obtained. By taking the assembled design as an example, as shown in **Figure 6a**, by introducing an offset δ , defined as the distance between the axes of the key-channels and the midlines of the center piece in the x–y plane, a new design with rotational symmetry about z axis is generated. Thus, due to the offsets, the forces applied on the center piece through the key-channels will generate a torque about the z axis. Also, due to the

sliding between keys and channels, auxetic effects also preserved. Then, under compression along z direction, the rotationally symmetric design will twist and shrink simultaneously.

The rigid components of the rotational symmetric design are fabricated via the 3D printer and the same springs are installed inside the channels. The assembled specimen is shown in Figure 6a. To experimentally characterize this unique behavior of coupled twisting and shrinkage, special fixtures are designed and fabricated to ensure correct boundary constraints, as shown in Figure 6b. To allow free shrinkage on the top and bottom surfaces, rigid fixtures with sliding channels in two orthogonal directions are designed and 3D printed, and matching keys are printed on the top and bottom surfaces of the specimen. Lubrication is applied between the keys and channels, ensuring free sliding and therefore the free shrinkage in the x-y plane. To ensure free twist-

www.advancedsciencenews.com

ADVANCED MATERIALS

vww.advmat.de

15214095, 2024, 15, Downloaded from https://onlinelibrary.wiley.com/doi/10.1002/adma.202309604 by Yaning Li - Northeastern University , Wiley Online Library on [30.062024]. See the Terms and Conditions (https://

-and-conditions) on Wiley Online Library for rules of use; OA articles are governed by the applicable Creative Commons

ing on top surface, a ball bearing is used to allow free rotation about z axis on the top surface. The rotation of the bottom surface is constrained by adding sandpaper between the specimen and the bottom compression disk. The twisting angle can be measured by a protractor attached to the top surface.

The experimental and FE results of the engineering stressstrain curves, the twisting angle, and the effective Poisson's ratio v_{zx} match well, as shown in Video S5 (Supporting Information) and Figure 6c.d. respectively. It can be seen that the twisting angle increases with the overall compressive strain, while the Poisson's ratio decreases with the overall compressive strain. Snapshots from the experiments and simulations at the overall compressive strains of 0, 0.04, 0.08, and 0.12 are shown in Figure 6e. The FE contours of the total displacement demonstrate the simultaneous in-plane rotation and shrinkage from both a 3D side view and a top view, as shown in Figure 6e. It is clearly seen that the 3D keyed-octahedron-cuboctahedron metamaterial shows coupled twisting and shrinking under uni-axial compression, as is rarely seen in existing mechanical metamaterials. It is known that materials with coupled twisting and axial deformation have a wide variety of applications in soft robotics.[21] mechanical computing devices, [22] sensors, and actuators. [23] The current design with simultaneous axial-twisting and axial-shrinking can further broaden these applications. For example, applications on soft robotic joints with tunable and controllable rotation and shrinkage, mechanical computing units for multi-digital logics, and devices that guide force filed or mechanical waves around obstacles.

3. Conclusions

In summary, a strategy of designing a new family of 3D auxetic tiled metamaterials based on 3D space filling tessellation is demonstrated via 3D keyed-octahedron-cuboctahedron designs, including the isotropic design, anisotropic design, and the rotationally symmetric design. Two types of designs are explored: the assembled designs with springs and the assembly-free design with double-ring connections. The former can be fabricated by assembling metal springs and 3D printed components, and the latter can be directly printed via a multi-material 3D printer. An integrated experimental, analytical, and numerical approach is applied to systematically quantify the unique mechanical properties of the new designs. Due to the remarkable and unusual mechanical properties and behaviors of this new family of mechanical metamaterials, they can have broad applications in soft robotics, mechanical actuators and dampers, and engineering materials/systems for energy absorption and impact and vibration mitigation.

Generally, the new metamaterials show large auxeticity together with remarkable resilience and significant hysteresis under cyclic loading–unloading compressive experiments. Both the effective stiffness and the damping ratio can be tuned via varying the friction coefficient between the 3D printed keys and channels. Three deformation stages separated by two contact events are identified during the loading process. The effective stiffness and the Poisson's ratio vary at different deformation stages. Stage II is the dominant stage for high auxeticity, resilience, and mechanical hysteresis. Depending on the friction coefficient, the designs show two deformation modes: sliding and locking. The critical friction coefficient for the transition from one mode to the

other is derived analytically and verified numerically and experimentally as well.

Interestingly, the isotropic design is proved to have ideal mechanical isotropy, including both effective stiffness and the negative Poisson's ratio close to -1, in all loading directions in the 3D space, as rarely seen in existing mechanical metamaterials. Compared with the existing auxetic mechanical metamaterials, the current isotropic design can increase the ratio between shear modulus and bulk modulus by order of magnitude, reaching the theoretical limit.

Also, by varying the orientation of the key-channel pairs, anisotropic designs can be created. The anisotropic mechanical properties including the effective stiffness and effective Poisson's ratio can be tuned in a very wide range. Design space for sliding or locking behaviors of the anisotropic designs are also explored and identified as a function of friction coefficient and the key-channel orientation.

In addition, by introducing an offset of the key-channel pairs, 3D rotationally symmetric designs can be created, which show a unique coupled compression, twisting, and shrinking behavior. To characterize this unique behavior, mechanical compression experiments on 3D printed specimens with specially designed fixtures are performed. The new designs have broad applications in soft robotics, mechanical actuators and dampers, and engineering materials/systems for energy absorption and impact and vibration mitigation.

4. Experimental Section

Mechanical Experiments: Each part of the assembly sample shown in Figure 2b and Figure S1 (Supporting Information) were manufactured by a multi-material 3D printer (Stratasys, Objet260) using a glassy polymer VeroClear and a soft rubbery material TangoPlus. VeroClear was used to print components of key and channel parts and TangoPlus was used to print the bumps on channels and keys to connect the metal springs. Each design of 3D metamaterial was assembled from the 3D printed parts and metal springs. The assembly-free samples shown in Figure 2c and Figure S2 (Supporting Information) were directly printed by the same 3D printer using a glassy polymer VeroWhite and soft rubbery material TangoBlack. VeroWhite was used to print components of key and channel parts and TangoBlack was used to print the double rings connection parts (Details can be found in Section S1, Supporting Information).

Uniaxial compression experiments were performed on each specimen by using an Instron universal material testing machine with a 500 N load cell. All experiments were conducted under a constant strain rate of $0.001\ s^{-1}$. To avoid the friction between the samples and compression plates, lubricating oil was used on the top and bottom surfaces of the samples. Markers were made on each specimen. A high-resolution camera (Grasshooper3) was used to record the deformed configurations of the specimens at each time instant during the experiments. By post-processing images, the displacement history of each marker point was obtained from which the effective Poisson's ratio and the overall strains were obtained.

Finite Element Simulations: Finite element (FE) models of the designs were developed in ABAQUS/CAE v 6.13. 3D tetrahedral elements (C3D10) were used, and the accuracy was verified by mesh refinement study. In the FE models, the 3D printed parts (VeroClear and VeroWhite) were modeled as isotropic, elastic-perfect–plastic material with Young's modulus of 1.4 GPa, the Poisson's ratio of 0.33, and the yielding stress of σ_y = 40 MPa. The constituent material for the metal spring was modeled as elastic-perfect–plastic material with Young's modulus of 207 GPa, the Poisson's ratio of 0.33, and the yielding stress of 2 GPa. The constituent material for the double rings (TangoBlack) was modeled as hyperelastic



www.advancedsciencenews.com

ADVANCED MATERIALS

www.advmat.de

15214095, 2024,

. 15, Downloaded from https://onlinelibrary.wiley.com/doi/10.1002/adma.202309604 by Yaning Li - Northeastern University , Wiley Online Library on [30/06/2024]. See

the Terms

and Condit

on Wiley Online Library for rules of use; OA articles are

governed by the

applicable

incompressible Neo-hooken model (C10 = 0.33 MPa, D1 = 0). In all FE models, the nonlinear geometry effect was considered. The contact between the key and channel parts was defined. To model the 3D printed materials, the friction coefficient was set as 0.53 by a systematic exploration. For the isotropic and anisotropic designs, numerical results were based on unit cell analysis with periodic boundary conditions. For the rotationally symmetric design, the boundary conditions of the FE model were the same as those applied in experiments. The displacement was controlled through the motion of the master nodes. Details of determining the elastic parameters through FE simulations can be found in Sections S4 and S5 (Supporting Information).

Supporting Information

Supporting Information is available from the Wiley Online Library or from the author.

Acknowledgements

This work was supported by the start-up funding and the SPARK funding from Northeastern University for Y.L. and National Science Foundation (NSF) via grant CMMI-2140223.

Conflict of Interest

The authors declare no conflict of interest.

Author Contributions

T.L. and Y.L. designed the experiments and simulations. Y.L. initiated the concept. T.L. conducted the experiments, finite element, and analytical analysis. T.L. and Y.L. interpreted the results. Y.L. supervised the overall research. Both authors contributed to the writing of the manuscript.

Data Availability Statement

The data that support the findings of this study are available in the supplementary material of this article.

Keywords

3D tiled auxetic metamaterial, hysteresis, isotropy, resilient, twist

Received: September 17, 2023 Revised: November 28, 2023 Published online: January 10, 2024

[1] a) X. Fang, J. Wen, L. Cheng, D. Yu, H. Zhang, P. Gumbsch, Nat. Mater. 2022, 21, 869; b) K. K. Dudek, J. A. I. Martínez, G. Ulliac, M. Kadic, Adv. Mater. 2022, 34, 2110115; c) X. Kuang, S. Wu, Q. Ze, L. Yue, Y. Jin, S. M. Montgomery, F. Yang, H. J. Qi, R. Zhao, Adv. Mater. 2021, 33, 2102113.

- [2] a) G. Lee, D. Lee, J. Park, Y. Jang, M. Kim, J. Rho, Commun. Phys. 2022, 5, 94; b) T. Tan, Z. Yan, H. Zou, K. Ma, F. Liu, L. Zhao, Z. Peng, W. Zhang, Appl. Energy 2019, 254, 113717.
- [3] a) H. Cheng, X. Zhu, X. Cheng, P. Cai, J. Liu, H. Yao, L. Zhang, J. Duan, Nat. Commun. 2023, 14, 1243; b) C. M. Portela, A. Vidyasagar, S. Krödel, T. Weissenbach, D. W. Yee, J. R. Greer, D. M. Kochmann, Proc. Natl. Acad. Sci. U. S. A. 2020, 117, 5686; c) H. Ryu, H. J. Yoon, S. W. Kim, Adv. Mater. 2019, 31, 1802898.
- [4] a) S. A. Cummer, J. Christensen, A. Alù, Nat. Rev. Mater. 2016, 1, 16001; b) N. Gao, Z. Zhang, J. Deng, X. Guo, B. Cheng, H. Hou, Adv. Mater. Technol. 2022, 7, 2100698.
- [5] a) C. M. Portela, B. W. Edwards, D. Veysset, Y. Sun, K. A. Nelson, D. M. Kochmann, J. R. Greer, Nat. Mater. 2021, 20, 1491; b) L. Jin, R. Khajehtourian, J. Mueller, A. Rafsanjani, V. Tournat, K. Bertoldi, D. M. Kochmann, Proc. Natl. Acad. Sci. U. S. A. 2020, 117, 2319; c) T. Frenzel, C. Findeisen, M. Kadic, P. Gumbsch, M. Wegener, Adv. Mater. 2016, 28, 5865.
- [6] a) G. N. Greaves, A. L. Greer, R. S. Lakes, T. Rouxel, Nat. Mater. 2011, 10, 823; b) R. Lakes, Science 1987, 235, 1038; c) R. H. Baughman, J. M. Shacklette, A. A. Zakhidov, S. Stafström, Nature 1998, 392, 362; d) B. Jenett, C. Cameron, F. Tourlomousis, A. P. Rubio, M. Ochalek, N. Gershenfeld, Sci. Adv. 2020, 6, eabc9943.
- [7] a) T. Li, Y. Li, Int. J. Solids Struct. 2022, 254–255, 111947; b) T. Li, Y. Li, J. Appl Mech 2022, 89, 101006.
- [8] a) T. Frenzel, M. Kadic, M. Wegener, Science 2017, 358, 1072; b) I. Fernandez-Corbaton, C. Rockstuhl, P. Ziemke, P. Gumbsch, A. Albiez, R. Schwaiger, T. Frenzel, M. Kadic, M. Wegener, Adv. Mater. 2019, 31, 1807742
- [9] a) T. A. M. Hewage, K. L. Alderson, A. Alderson, F. Scarpa, Adv. Mater. 2016, 28, 10323; b) S. Shan, S. H. Kang, J. R. Raney, P. Wang, L. Fang, F. Candido, J. A. Lewis, K. Bertoldi, Adv. Mater. 2015, 27, 4296.
- [10] a) Q. Wang, J. A. Jackson, Q. Ge, J. B. Hopkins, C. M. Spadaccini, N. X. Fang, Phys. Rev. Lett. 2016, 117, 175901; b) L. Wu, B. Li, J. Zhou, ACS Appl. Mater. Interfaces 2016, 8, 17721.
- [11] S. Zanotto, G. Biasiol, P. V. Santos, A. Pitanti, Nat. Commun. 2022, 13, 5939.
- [12] R. O. Ritchie, Nat. Mater. 2011, 10, 817.
- [13] a) R. Lakes, Viscoelastic Materials, 1st ed., Cambridge University Press, Cambridge 2009; b) P. Zhang, M. A. Heyne, A. C. To, J. Mech. Phys. Solids 2015, 83, 285.
- [14] L. J. Gibson, M. F. Ashby, Cellular Solids: Structure and Properties, 2nd ed., Cambridge University Press, Cambridge 1997.
- [15] T. A. Schaedler, W. B. Carter, Annu. Rev. Mater. Res. 2016, 46, 187.
- [16] a) S. Shan, S. H. Kang, Z. Zhao, L. Fang, K. Bertoldi, Extreme Mech. Lett. 2015, 4, 96; b) J. B. Berger, H. N. G. Wadley, R. M. McMeeking, Nature 2017, 543, 533; c) T. Tancogne-Dejean, M. Diamantopoulou, M. B. Gorji, C. Bonatti, D. Mohr, Adv. Mater. 2018, 30, 1803334.
- [17] B. Grünbaum, Geombinatorics 1994, 4, 49.
- [18] K. E. Evans, A. Alderson, Adv. Mater. 2000, 12, 617.
- [19] a) T. Y. Thomas, Proc. Natl. Acad. Sci. U. S. A. 1966, 55, 235; b) Z. Jia, L. Wang, Phys. Rev. Appl. 2019, 12, 024040; c) J. Turley, G. Sines, J. Phys. D: Appl. Phys. 1971, 4, 264.
- [20] a) J. Liu, Y. Zhang, Soft Matter 2018, 14, 693; b) D. Li, G. Shen, Smart Mater. Struct. 2022, 31, 065017.
- [21] J. Liu, X. Wang, S. Liu, J. Yi, X. Wang, Z. Wang, IEEE Robot Autom Lett 2022, 7, 658.
- [22] H. Yasuda, P. R. Buskohl, A. Gillman, T. D. Murphey, S. Stepney, R. A. Vaia, J. R. Raney, *Nature* **2021**, *598*, 39.
- [23] X. Tan, J. A. I. Martínez, G. Ulliac, B. Wang, L. Wu, J. Moughames, M. Raschetti, V. Laude, M. Kadic, Small 2022, 18, 2202128.